ACS Catalysis

Research Article

pubs.acs.org/acscatalysis

Tuning Catalytic Selectivity of Oxidative Catalysis through Deposition of Nonmetallic Atoms in Surface Lattice of Metal Oxide

Juanjuan Liu,[†,‡,⊥] Shiran Zhang,[†,⊥] Yan Zhou,[§,⊥] Victor Fung,[∥] Luan Nguyen,[†] De-en Jiang,[∥] Wenjie Shen,[§] Jie Fan,[*,‡] and Franklin Feng Tao[*,†]

[†]Department of Chemical and Petroleum Engineering and Department of Chemistry, University of Kansas, Lawrence, Kansas 66045, United States

[‡]Department of Chemistry, Zhejiang University, Hangzhou 310027, China

[§]State Key Laboratory of Catalysis, Dalian Institute of Chemical Physics, Chinese Academy of Sciences, Dalian 116023, China

[∥]Department of Chemistry, University of California, Riverside, California 92521, United States

ABSTRACT: Catalytic selectivity for producing an ideal product is a key topic for chemical transformations through heterogeneous catalysis. Tuning catalytic selectivity by integrating the second metal to form an alloy has been well demonstrated in the literature. Here we report a method to tune catalytic selectivity in oxidative catalysis on another category of heterogeneous catalysts, transition-metal oxides. By choosing the oxidative dehydrogenation (ODH) of ethane to ethylene as a probe reaction, we demonstrated that doping nonmetallic atoms to the surface lattice of catalyst of a transition-metal oxide can enhance catalytic selectivity through suppression of complete oxidation of the reactant molecules. Catalysts of Co_3O_4 with doped silicon atoms (Si_x-Co_3O_4) maintaining the spinel structure of pure Co_3O_4 exhibit much higher selectivity for the production of ethylene through ODH of ethane in comparison to pure Co_3O_4 at 600 °C by 40%. The suppression of activity of surface lattice oxygen atoms was evidenced by the observation that the surface lattice oxygen atoms of Si_x-Co_3O_4 cannot exchange oxygen atoms with gas-phase oxygen at low temperatures while pure Co_3O_4 can. The difference in releasing surface lattice oxygen atoms and dissociating molecular oxygen between pure Co_3O_4 and Si_x-Co_3O_4 was supported by DFT calculations. The calculated activation barriers for dissociation of molecular O_2 and energy barriers for hopping surface oxygen vacancies of Si_x-Co_3O_4 are obviously higher than those of pure Co_3O_4, respectively. These experimental exploration and computational studies established a correlation between increase of catalytic selectivity and suppression of the activity of surface lattice oxygen atoms/oxygen vacancies. This correlation suggests an approach for increasing the catalytic selectivity of oxidative catalysis through suppressing activity of surface lattice oxygen atoms/vacancies via doping atoms of a nonmetallic element. This new approach was further confirmed by the observed higher catalytic selectivity for production of ethylene on $Ge_{0.2}$-Co_3O_4 in comparison to pure Co_3O_4.

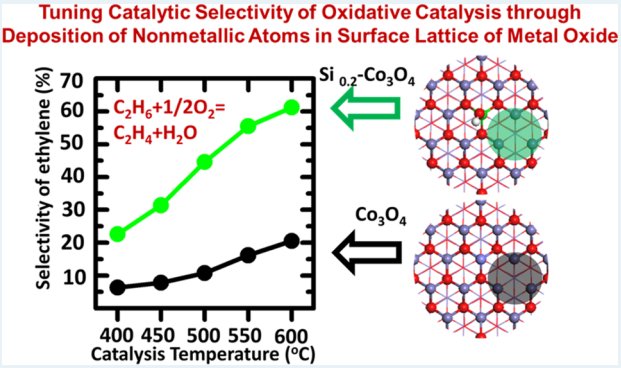

KEYWORDS: *catalytic selectivity, oxidative dehydrogenation, ethane, ethylene, surface lattice oxygen, oxygen vacancies, cobalt oxide*

1. INTRODUCTION

Tuning catalytic selectivity is the key for green production in chemical and energy transformations.[1−4] Catalytic oxidation is one of the main categories of heterogeneous catalysis in chemical production. Except for a complete oxidation such as combustion of hydrocarbons,[5] partial oxidation or selective oxidation for production of an ideal product remains challenging in heterogeneous catalysis, since deep oxidation such as complete oxidation is typically a side reaction which results in a low selectivity for the channel of a partial oxidation or selective oxidation. The design of a catalyst with high selectivity for production of an ideal product is the goal of most efforts in fundamental studies of oxidative catalysis.[6,7] For oxidative catalysis on a metal at a relatively low temperature, the activation barrier for dissociation of molecular oxygen could be largely tuned through alloying it with a second metal.[8−11] This capability is closely related to the tuning of the d-band center of the host metal by alloying it with a second metal. However, for oxidative catalysis at a high temperature, the method of tuning catalytic performance through formation of an alloy may not work, as the alloy could be readily oxidized into a metal oxide at a high reaction temperature. Thus, a method to tune the catalytic performance of oxidative catalysis on a metal oxide is highly demanded.

Ethylene is one of the most important building blocks of chemical industries. It is widely used as a feedstock for

Received: December 19, 2015
Revised: April 27, 2016
Published: June 6, 2016

Downloaded via GEORGIA INST OF TECHNOLOGY on September 14, 2022 at 19:19:38 (UTC).
See https://pubs.acs.org/sharingguidelines for options on how to legitimately share published articles.

© 2016 American Chemical Society

DOI: 10.1021/acscatal.5b02900
ACS Catal. 2016, 6, 4218−4228

production of various polymers and other important raw materials in industries.[12−15] The catalytic transformation of ethane to ethylene through oxidative dehydrogenation (ODH) is one of the most important building blocks of the library of new chemical processes being developed as the current petroleum-based production processes are being shifted to shale gas-based processes. In comparison to pyrolysis of ethane to produce ethylene at 700−900 °C, the low-temperature ODH of ethane process at 400−600 °C can significantly save energy in the production of ethylene.[16−23] In this work, we chose the ODH of ethane for the production of ethylene as a probe reaction to explore how catalytic selectivity of an oxidative catalytic reaction on a reducible oxide could be tuned through doping atoms of a nonmetallic element.

The main side reaction of ODH of ethane is the complete oxidation of ethane to CO_2 and H_2O, since a complete oxidation is more thermodynamically favorable than ODH. Another side reaction is partial oxidation of some intermediates (formed in the pathway of ODH) to CO and H_2O. Thus, an ideal catalyst of ODH of ethane for production of ethylene is inactive for both a complete oxidation of ethane to CO_2 and a partial oxidation of intermediates of ODH to CO. Although numerous catalysts for ODH of ethane have been reported,[24−29] most catalysts except MoVTe(Sb)NbO (M1 catalyst)[30−33] and Ni−Nb−O[34−36] do not exhibit a high selectivity. Control of the extent of oxidation of ethane toward a high catalytic selectivity for the production of ethylene remains significantly challenging.

For a catalyst consisting of a reducible oxide, surface lattice oxygen atoms play a significant role in activation of C−H and formation of an OH intermediate in the ODH, although the type of oxygen species of surface lattice participating into the action of ODH is still unknown. Other than the pathway of ODH, they are significantly involved in coupling with intermediates of the ODH pathway to form CO_2 in a complete oxidation or form CO in partial oxidation. From a surface structure point of view, the activity of surface lattice oxygen atoms was hypothesized to be a key descriptor for the catalytic selectivity for production of ethylene. Thus, tuning of chemical states of surface oxygen vacancies and surface lattice oxygen atoms toward optimizing their roles in selective oxidation to form ethylene instead of CO and CO_2 is hypothesized to be one approach to promote the catalytic selectivity for production of ethylene.

To test this hypothesis, Co_3O_4 was chosen as a probe catalyst, since it is active for oxidation of hydrocarbons such as methane and others;[5] likely, a suppression of the high activity of surface oxygen vacancies in dissociating molecular oxygen in terms of weakening the capability of releasing surface lattice oxygen atoms could promote the catalytic selectivity for production of ethylene. To suppress the high activity of surface lattice oxygen atoms of Co_3O_4, a non-transition-metal element, here the nonmetallic element silicon, was chosen since it bonds to oxygen atoms much more strongly than cobalt. It is expected that doping silicon atoms could decrease the activity of surface lattice oxygen atoms/oxygen vacancies in the partial oxidation of intermediates to CO and H_2O or/and complete oxidation of ethane to CO_2 and H_2O and thus promote catalytic selectivity for the production of ethylene through ODH.

In this work, pure Co_3O_4 and doped Co_3O_4 (Si_x-Co_3O_4, x = the nominal molar ratio of Si to Co) were synthesized. Their catalytic performances were studied under the same catalytic conditions. It is found that Si_x-Co_3O_4 exhibits higher selectivity than pure Co_3O_4, up to 40% at the same temperature. The suppression of the activity of the Co_3O_4 surface in releasing surface lattice oxygen atoms and generating surface oxygen vacancies by doping silicon atoms was confirmed with isotope exchange experiments. DFT calculations supported the differences in dissociating molecular oxygen and hopping surface oxygen vacancies between pure Co_3O_4 and Si_x-Co_3O_4, suggesting that the low activity of surface lattice oxygen atoms/oxygen vacancies of Si_x-Co_3O_4 is responsible for the high selectivity for production of ethylene and low selectivity for production of CO or/and CO_2. A similar promotion effect of catalytic selectivity for production of ethylene was observed on Ge-doped Co_3O_4. Thus, the significant increase of catalytic selectivity for selective oxidation by doping atoms of a nonmetallic element demonstrated a new approach of increasing selectivity in oxidative catalysis.

2. EXPERIMENTAL AND COMPUTATIONAL SECTION

2.1. Synthesis of Pure Co_3O_4 Catalyst. Pure Co_3O_4 nanorods were synthesized by a method reported in the literature.[37,38] Briefly, 2.49 g of cobalt acetate tetrahydrate was dissolved in 30 mL of ethylene glycol and then the mixture was heated to 160 °C with vigorous stirring under an N_2 atmosphere. A 100 mL portion of a 0.20 M Na_2CO_3 aqueous solution was added to the mixture dropwise (1.11 mL min^{-1}). Then, the solution was refluxed for 1 h. Centrifugation of the mixture gave a purple product, which was then dried at 50 °C overnight in a vacuum oven. Co_3O_4 catalyst was obtained by a subsequent calcination in air at 350 °C for 4 h.

2.2. Synthesis of Si-Doped Co_3O_4 Catalysts. Typically, 0.30 g of prepared Co_3O_4 nanorods, 40 mL of ethanol, and 2 mL of concentrated ammonium hydroxide were mixed. The mixture was continuously stirred. Then 20 mL of ethanol with tetraethyl orthosilicate (TEOS) was introduced into the above mixture by dropping slowly within 10 h. After the mixture was stirred vigorously for another 6 h, the black products were obtained by centrifugation. The as-synthesized materials were calcined at 350 °C in air for 2 h (ramping rate 2 °C min^{-1}) to obtain the surface-doped Co_3O_4 catalysts, which were labeled as Si_x-Co_3O_4 (x is the nominal molar ratio of Si to Co).

2.3. Synthesis of Ge-Doped Co_3O_4 Catalyst. Typically, 0.30 g of prepared Co_3O_4 nanorods, 40 mL of ethanol, and 2 mL of ammonia solution ($NH_3 \cdot H_2O$, 25−28%) were mixed. The mixture was stirred vigorously for 15 min, and then 20 mL of ethanol with germanium chloride ($GeCl_4$) was introduced into the above mixture by dropping slowly within 10 h. After the mixture was stirred vigorously for another 6 h, the black products were obtained by centrifugation. The as-synthesized materials were calcined at 350 °C in air for 2 h (ramping rate 2 °C min^{-1}) to obtain the surface-doped Co_3O_4 catalyst, which was labeled as Ge_y-Co_3O_4 (y is the nominal atomic ratio of Ge to Co).

2.4. Measurements of Catalytic Performances. All measurements of catalytic performances of ODH of different catalysts were performed in a fixed-bed reactor operating. They were conducted in the temperature range of 400−600 °C with 0.050 g of catalyst diluted with 0.50 g of quartz sand. Before use, the quartz sand was purified by aqua regia solution and then washed with deionized water several times. The inner diameter of the test tube in the reactor was 6 mm. The sources of the reactant gases were one gas cylinder of 10.0% C_2H_6/Ar (cylinder 1) and one gas cylinder of 10.0% O_2/Ar (cylinder 2). Flows of 25 mL min^{-1} of 10.0% C_2H_6 from cylinder 1 and 25 mL min^{-1} 10.0% O_2 from cylinder 2 were mixed and then introduced to the fixed-bed flow reactor. The gas composition of the mixture of reactant gases entering this fixed-bed flow reactor was 5/5/90 for C_2H_6/O_2/Ar. The weight to flow ratio (weight of catalyst)/(total gas flow rate) is 0.060 g s mL^{-1}. Ethane and reaction products were analyzed online with a gas chromatograph equipped with a FID detector. Blank experiments were performed on 0.55 g of quartz sand in the same fixed-bed flow reactor while the mixture of reactants was introduced. Conversions of <1.0% at 400 °C and of <2.0% at 600 °C were found for the 0.55 g quartz sand. Experimental errors of the measurements of conversion and selectivity are ±5% of the reported conversion and selectivity, respectively. Carbon balances were in the range of 100 ± 5%.

DOI: 10.1021/acscatal.5b02900
ACS Catal. 2016, 6, 4218−4228

To interpret the suppression of surface atoms of Co_3O_4 by doping Si, complete oxidation of ethane to CO/H_2O and/or CO_2/H_2O was conducted between 200 and 600 °C on 0.050 g of catalyst diluted with 0.50 g of purified quartz sand. The reactant gases were 10.0% C_2H_6/Ar (10 mL min^{-1}) and 10.0% O_2/Ar (40 mL min^{-1}). The feedstock composition was 2/8/90 for C_2H_6/O_2/Ar. The weight to flow ratio (W/F) was 0.060 g s mL^{-1}. Ethane and ethylene were analyzed with an online gas chromatograph equipped with an FID detector.

2.5. Characterizations. Powder X-ray diffraction (XRD) patterns were recorded on a Rigaku Ultimate IV operating in reflection mode with Cu Kα radiation that was monochromated with a secondary graphite monochromator. The nitrogen sorption measurements were performed on a Micromeritics (2010 unit) at 77 K. The Si (doped)/Co atom ratio was calculated with the equation

$$\frac{A_{\mathrm{Si\ 2p(doped)}}/S_{\mathrm{Si\ 2p}}}{A_{\mathrm{Co\ 2p}}/S_{\mathrm{Co\ 2p}}}$$

where A and S stand for the peak area and sensitivity factor of a subshell, respectively. HAADF-STEM imaging and EDX analysis were performed on a JEOL Arm 200F instrument at 200 kV.

Temperature-programmed reduction (H_2-TPR) was carried out with a Micromeritics Autochem 2910 instrument equipped with a TCD detector; typically, the catalyst sample (20 mg) was placed in a U-shaped quartz reactor and pretreated in flowing Ar for 1 h at 120 °C, followed by cooling to room temperature; the temperature was then raised from room temperature to 800 °C at a rate of 10 °C min^{-1} in a 5.0% H_2/Ar flow (total flow rate 30 mL min^{-1}).

The oxygen isotope exchange experiments were conducted using a fixed-bed flow reactor coupled to a quadrupole mass spectrometer for online measurements of the gases in the fixed-bed flow reactor. The quadrupole mass spectrometer can readily distinguish $^{16}O_2$ (m/z 32), $^{18}O_2$ (m/z 36), and $^{16}O^{18}O$ (m/z 34). Pure Co_3O_4 or Si_x-Co_3O_4 was annealed at 500 °C in an $^{18}O_2$ atmosphere for 0.5 h and then cooled to 30 °C to generate an isotope-labeled catalyst. The sample was then purged with N_2 for 1 h at 30 °C to eliminate the $^{18}O_2$, $^{16}O^{18}O$, and $^{16}O_2$ until the mass spectrometer signals of $^{18}O_2$, $^{16}O^{18}O$, $^{16}O_2$ returned to the baseline. Then, 5.0% $^{16}O_2$ was introduced to flow through the catalyst; the temperature was raised from 30 to 600 °C at a heating rate of 20 °C min^{-1} to perform a potential oxygen exchange between ^{16}O and ^{18}O. When one peak appeared at the temperature T_0, the sample was then continued to be annealed until there was no further increase in the intensity of $^{16}O^{18}O$ at the temperature T_m; then, the sample was kept at T_m until there was no more $^{16}O^{18}O$ formed. In other words, the signal of $^{16}O^{18}O$ went back to the original baseline. Then, the catalyst was annealed to a higher temperature with a ramping rate of 20 °C min^{-1} until the next peak appeared.

2.6. Computational Method. Computational studies were performed to interpret how the doping of silicon atoms suppresses the complete oxidation of ethane and thus enhances the selectivity for production of ethylene through ODH. All calculations were performed with density functional theory (DFT) using the Vienna ab initio simulation package (VASP).[39] The on-site Coulomb interaction was corrected using the DFT+U method by Dudarev et al.[40] in VASP using a Hubbard parameter of U = 2 eV for the cobalt. The Perdew–Burke–Erzerhof (PBE)[41] form of the generalized-gradient approximation (GGA) was chosen for electron exchange and correlation. The electron–core interaction was described using the projector-augmented wave method (PAW).[42] In the calculations spin polarization was considered, with a kinetic energy cutoff of 500 eV, and a Brillouin zone sampling using a 3 × 3 × 1 Monkhorst–Pack scheme. On the basis of the STEM image (see the next section), the (111) surface was preferentially exposed and therefore chosen to model surface chemistry and catalysis on pure and doped Co_3O_4. The slab was created containing 11 layers, with the bottom 9 layers frozen at their bulk positions.

3. RESULTS AND DISCUSSION

3.1. Doping of Silicon Atom to Surface Lattice of Co_3O_4. The doped Co_3O_4 catalysts of Si_x-Co_3O_4 (x = 0.1, 0.2, 0.4) were synthesized with a two-step method. Figure 1 presents the diffraction patterns of fresh and used Co_3O_4 or Si_x-Co_3O_4 (x = 0.1, 0.2, 0.4). Here the terms "fresh" and "used" stand for a catalyst sample before catalysis and after catalysis, respectively. In diffraction patterns of Si_x-Co_3O_4 (x = 0.1, 0.2, 0.4), only the Co_3O_4 phase was observed. Notably, diffraction patterns of SiO_2 are absent, though the concentration of silica is definitely higher than the sensitivity of the XRD analysis. The lack of any diffraction patterns of SiO_2 suggests a lack of crystallized silica resulting from a quite low annealing temperature in the preparation of Si_x-Co_3O_4. In fact, the annealing temperatures in both the preparation of Si_x-Co_3O_4 and the following catalysis temperatures are much lower than the required crystallization temperature of SiO_2 (>1000 °C).[43] The TEM images of Figure 2a and 2f show the morphology of the fresh $Si_{0.2}$-Co_3O_4 and used $Si_{0.2}$-Co_3O_4. EDX analysis of $Si_{0.2}$-Co_3O_4 shows that the atomic ratio of Si to Co is 18% (inset of Figure 2a), which is consistent with the atomic ratio of the precursors of silicon to cobalt used in the preparation of $Si_{0.2}$-Co_3O_4. The EDX mapping of the fresh and used $Si_{0.2}$-Co_3O_4 displays that the Si, O, and Co elements are highly dispersed on the whole $Si_{0.2}$-Co_3O_4 framework. Thus, the complementary information on XRD and EDX suggest that the introduced silicon atoms exist in the forms of amorphous silica surrounding Co_3O_4 or/and dopants of Co_3O_4.

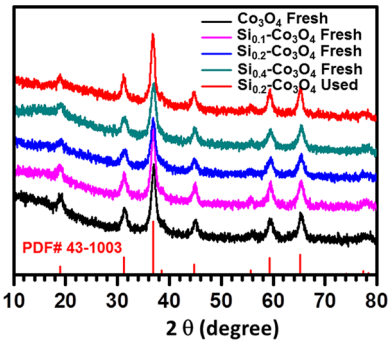

Figure 1. XRD patterns of fresh Si_x-Co_3O_4 catalysts (x = 0, 0.1, 0.2, 0.4) and of used $Si_{0.2}$-Co_3O_4.

The lattice fringe of the used $Si_{0.2}$-Co_3O_4 catalyst was clearly identified with an aberration corrected scanning transmission electron microscope (AC-STEM) at Arizona State University. Figure 2j shows the large area of used $Si_{0.2}$-Co_3O_4 catalyst and Figure 2k,l gives representative atom-resolved AC-STEM images. As shown in Figure 2l, the measured lattice fringes along the [02−2] and [2−20] directions are 2.80 and 2.80 Å, which are the same as those of pure Co_3O_4; the lack of change of lattice fringe in $Si_{0.2}$-Co_3O_4 suggests (1) the introduction of silicon atoms on or/and into Co_3O_4 mainly modified the lattice of surface region of Co_3O_4, since TEM provides information on the projection of the atomic column of an entire Co_3O_4 nanoparticle, and (2) only a portion of the silicon atoms of the precursors were doped on the surface lattice of Co_3O_4. The schematics of this process are shown in Figure 3. Figure 3b schematically shows $Si_{0.1}$-Co_3O_4. In addition, from the XRD data in Figure 1, there is a lack of change in the lattice constant of Si_x-Co_3O_4 along the increase of atomic ratio of Si to Co precursors, x, from 0.1 to 0.4. In other words, the rest of the silicon atoms must exist in the form of amorphous silica on doped Co_3O_4 (Figure 3c). Unfortunately, the amorphous SiO_2 is not identifiable in XRD data and is invisible in STEM due to the low Z value of Si in comparison to Co.

DOI: 10.1021/acscatal.5b02900
ACS Catal. 2016, 6, 4218−4228

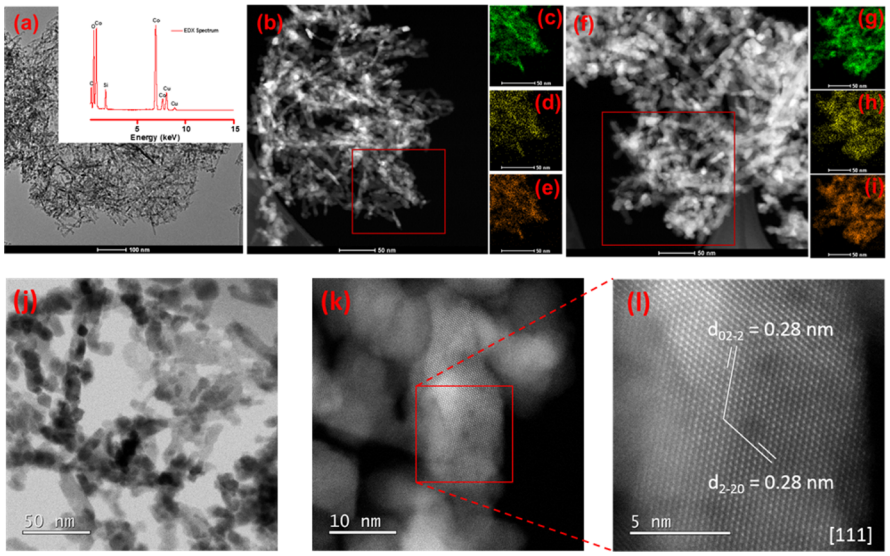

Figure 2. TEM studies of of fresh and used $Si_{0.2}$-Co_3O_4 catalysts. (a) Large-scale TEM image of fresh $Si_{0.2}$-Co_3O_4 catalyst. The inset is the EDX spectrum of an area of 500 nm. (b) HADDF-STEM image. The area marked with a red box was chosen for EDX mapping. (c–e) Mapping of Co K-edge, Si K-edge, and O K-edge of the marked area in (b). (f) HAADF-STEM image of used $Si_{0.2}$-Co_3O_4 catalyst. The red box is the chosen area for EDX mapping. (g–i) Mapping of Co K-edge, Si K-edge, and O K-edge of the marked area in (f). (j–l) Aberration corrector STEM images of used $Si_{0.2}$-Co_3O_4 catalyst: (j) large area of used $Si_{0.2}$-Co_3O_4 catalyst (after ODH of ethane at 600 °C); (k) small area of used $Si_{0.2}$-Co_3O_4 catalyst (after ODH of ethane at 600 °C); (l) representative high-resolution aberration corrector STEM image, with the lattice fringe readily identified.

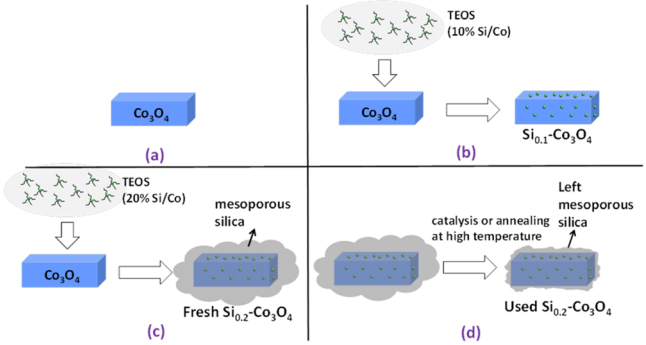

Figure 3. Schematics showing the introduction of silicon to the surface lattice of Co_3O_4 or/and the formation of a silica mesoporous shell and the evolution of the mesoporous shell during annealing or catalysis at high temperature. (a) Schematic of a pure Co_3O_4 nanorod. (b) Schematic of $Si_{0.1}$-Co_3O_4. The silicon atoms of the precursor were mainly doped on the surface lattice of Co_3O_4. (c) Schematic of the formation of $Si_{0.2}$-Co_3O_4. The preparation of $Si_{0.2}$-Co_3O_4 includes the introduction of precursor TEOS (20%) and the following calcination at 350 °C for 2 h; an amorphous mesoporous silica shell was formed on the Si-deposited Co_3O_4. (d) Collapse of the amorphous mesoporous silica shell after experiencing catalysis at 600 °C or being annealed at 600 °C in air. The collapsed silica occupied some portion of the surface of Co_3O_4.

The successful doping of silicon atoms on the surface lattice of Co_3O_4 and the modification of the electronic state of Co atoms of Co_3O_4 were suggested by the photoemission features of Co 2p and Si 2p of $Si_{0.2}$-Co_3O_4 shown in Figure 4. The photoemission feature of Co 2p of the pure Co_3O_4 (black line in Figure 4a) is consistent with the literature.[44] The main peak of Co 2p at ~780.0 eV is attributed to Co $2p_{3/2}$ of Co^{2+} and Co^{3+} of Co_3O_4. The small shoulder at about 789.8 eV is attributed to the satellite peak of Co $2p_{3/2}$ of Co^{3+} in an octahedral coordination with oxygen atoms in Co_3O_4.[45] In comparison to Co $2p_{3/2}$ of pure Co_3O_4 (black line in Figure 4a), the main peak of Co $2p_{3/2}$ of the used catalyst, $Si_{0.2}$-Co_3O_4 (blue line in Figure 4a), obviously upshifts by 0.7 eV. Notably, the upshift of Co $2p_{3/2}$ is not due to any surface charging because Si 2p of the same sample in the same XPS measurement indeed downshifts by 0.8 eV, in contrast to Si 2p of SiO_2/Si which was achieved from a SiO_2 thin film support on silicon wafer in Figure 4b. If there were surface charging of the used $Si_{0.2}$-Co_3O_4 due to low conductivity of the catalyst surface during XPS studies, photoemission peaks of Si 2p and Co 2p would have upshifted accordingly. Then, the opposing shifts of Co 2p and Si 2p of the used $Si_{0.2}$-Co_3O_4 definitely excluded the possibility of surface charging during XPS measurements.

The upshift of Co 2p and downshift of Si 2p suggest that electron density on Co atoms is transferred to Si atoms in the case of the used $Si_{0.2}$-Co_3O_4. Si 2p of the used $Si_{0.2}$-Co_3O_4 was deconvoluted into a peak contributed from the doped Si atoms (102.16 eV, peak B in Figure 4c) and another peak from the Si atoms of supported silica shell (103.09 eV, peak A in Figure 4c). The atomic ratio of the doped Si to Co of the surface region of the catalyst was calculated with XPS data to be about 0.60 (see calculation details in section 2.5) on the basis of a quantitative analysis. This ratio is much higher than the 18% of the bulk of $Si_{0.2}$-Co_3O_4 measured with EDX analysis (inset of Figure 2a). The obviouly higher atomic ratio of Si to Co in surface region of the used $Si_{0.2}$-Co_3O_4 (from XPS) in comparison to the ratio of the bulk of the same sample (from EDX) suggests the formation of a silica shell supported on silicon-doped Co_3O_4, as schematically shown in Figure 3c.

3.2. Formation of Mesoporous Amorphous Silica Shell on Co_3O_4. As described in the Experimental and Computational Section, silicon atoms of Si_x-Co_3O_4 catalysts were introduced by hydrolyzation of TEOS with a following calcination at 350 °C. On the basis of the literaure,[46] such a preparation typically forms a mesoporous amorphous silica shell. As the mesoporous silica shell reported in the literature has a high surface area,[47] it is expected that the surface areas of Si_x-Co_3O_4 catalysts are higher than that of pure Co_3O_4. Table 1 gives the measured surface areas of Co_3O_4, $Si_{0.1}$-Co_3O_4, and $Si_{0.2}$-Co_3O_4. As expected, the surface

DOI: 10.1021/acscatal.5b02900
ACS Catal. 2016, 6, 4218–4228

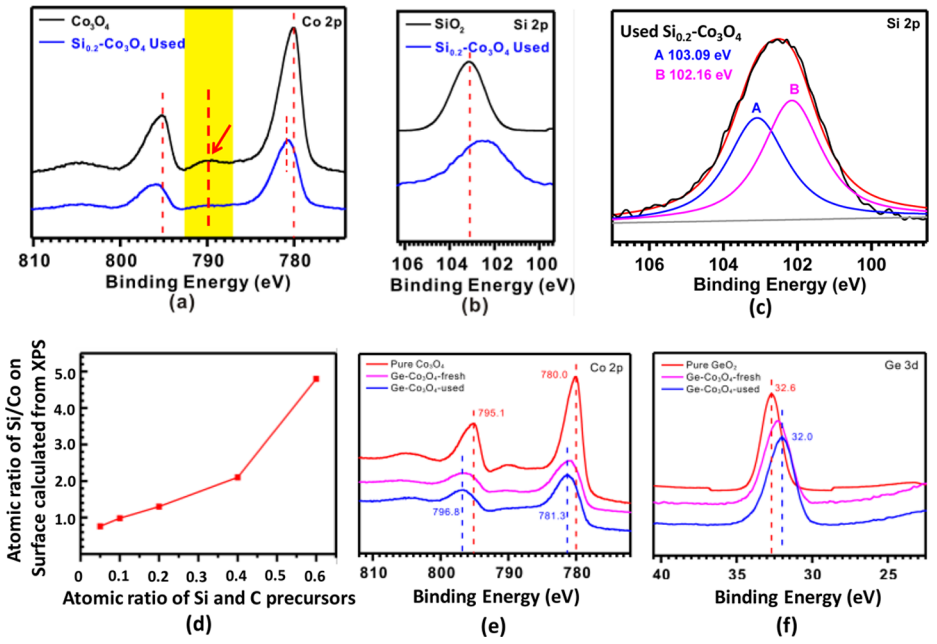

Figure 4. Photoemission features of Co 2p and Si 2p of the Co_3O_4 and used Si_x-Co_3O_4 catalysts and Co 2p and Ge 3d of fresh and used Ge-Co_3O_4. (a) Co 2p spectra of Co_3O_4 and the used $Si_{0.2}$-Co_3O_4. (b) Si 2p spectra of SiO_2/Si and used $Si_{0.2}$-Co_3O_4. (c) Deconvolution of Si 2p of the used $Si_{0.2}$-Co_3O_4 into two peaks with equal fwhm at 103.09 and 102.16 eV, respectively. (d) Plot of Si/Co atomic ratio of Si and Co precursors used in synthesis of Si_x-Co_3O_4 samples (x = 0.05, 0.1, 0.2, 0.4, 0.6). (e) Photoemission features of Co 2p of the pure Co_3O_4 (red), fresh Ge-Co_3O_4 (pink), and used Ge-Co_3O_4 (blue). (f) Photoemission features of Ge 3d of the pure GeO_2/Ge wafer (red), fresh $Ge_{0.2}$-Co_3O_4 (pink), and used $Ge_{0.2}$-Co_3O_4 (blue).

Table 1. Surface Areas of Fresh and Used Catalysts

		surface area (m^2 g^{-1})	
entry	catalyst	fresh	used
1	Co_3O_4	118.1	56.0
2	$Si_{0.1}$-Co_3O_4	118.9	99.8
3	$Si_{0.2}$-Co_3O_4	158.7	103.8
4	$Si_{0.2}$-Co_3O_4[a]	112.1	N/A[b]

[a]Calculated at 600 °C in O_2. [b]The catalyst $Si_{0.2}$-Co_3O_4 (annealed in O_2 at 600 °C) was not used for catalysis, and thus its surface area is not available.

area of fresh $Si_{0.2}$-Co_3O_4 is 42% higher than that of fresh Co_3O_4. In comparison to fresh pure Co_3O_4, however, the fresh $Si_{0.1}$-Co_3O_4 catalyst only exhibits a similar surface area. The negligible increase in surface area after the introduction of the first 10% of silicon atoms in the preparation of $Si_{0.1}$-Co_3O_4 suggests that the first 10% of silicon atoms were likely doped on the surface lattice of Co_3O_4 nanoparticles (Figure 3b). In other words, the first 10% does not form a mesoporous shell. In comparison to the fresh $Si_{0.1}$-Co_3O_4 catalyst, the obvious increase in surface area of the fresh $Si_{0.2}$-Co_3O_4 in contrast to the fresh Co_3O_4 shows that the majority of the second 10% of the added silicon precursor molecules have formed a mesoporous amphorous shell on doped Co_3O_4 (Figure 3c). In addition, we also collected XPS data for Si_x-Co_3O_4 (x = 0.05, 0.1, 0.2, 0.4, 0.6) as a function of Si concentration to investigate the interactions between Si and Co. As shown in Figure 4d, the surface Si/Co molar ratio varies with the Si/Co atomic ratio of silicon and cobalt precursors used in synthesis. When the Si/Co precursor molar ratio is lower than 0.4, the *surface* Si/Co ratio increases almost linearly with the Si concentration; the slope of the plot (Figure 4d) is greater than 1.0. This suggests that the added silicon precursor tends to form a silica shell on the surface of Co_3O_4 instead of forming SiO_2 particles alone. If separated SiO_2 nanoparticles were formed, the surface ratio Si/Co measured with XPS would not increase along with an increase in the Si/Co ratio of precursors; this is because the separated SiO_2 nanoparticles could not cover the Co_3O_4 nanoparticles to block photoelctrons generated from the surface of Co_3O_4 nanoparticles. Thus, the linear increase of surface Si/Co molar ratio excludes the formation of SiO_2 nanoparticles. A sharp increase of surface Si/Co molar ratio to 5.0 was observed when the Si/Co molar ratio of precursors is 0.6; this suggests that the shell is thick and most of the surface Co atoms can be covered by the silica shell.

The differences between the measured surface areas of fresh catalysts and those of the used catalysts in Table 1 further suggest the formation of a mesoporous amphorous silica shell on Co_3O_4 nanoparticles. The decrease in surface area of the fresh pure Co_3O_4 (118.1 m^2 g^{-1}) to 56.0 m^2 g^{-1} for the used Co_3O_4 catalyst (Table 1) suggests that pure Co_3O_4 was sintered after the catalysis at 600 °C. In comparison to the significant decrease in surface area of fresh pure Co_3O_4 after catalysis by 44%, however, the surface area of $Si_{0.1}$-Co_3O_4 after catalysis only decreased by 15%. This suggests that the doped silicon atoms on Si_x-Co_3O_4 have prevented Co_3O_4 nanoparticles from sintering.

In terms of $Si_{0.2}$-Co_3O_4, the surface area largely decreased by 35% after catalysis. This decrease of 35% is significant in comparison to the decrease of only 15% of the surface area of $Si_{0.1}$-Co_3O_4 after catalysis. This obvious decrease of surface area of $Si_{0.2}$-Co_3O_4 after catalysis (Table 1) suggests the collapse of the mesoporous amphorous shell of $Si_{0.2}$-Co_3O_4 to some extent during catalysis at 600 °C (Figure 3d). In other words, the first 10% of silicon atoms in $Si_{0.1}$-Co_3O_4 or $Si_{0.2}$-Co_3O_4 were doped in surface lattices of Co_3O_4 instead of forming an obvious mesoporous amphorous shell. The high activity of $Si_{0.2}$-Co_3O_4 (Figure 5a) suggests that the collapsed mesoporous silica shell only covered a portion of the catalyst surface. To further confirm that the collapse of the mesoporous amorphous shell of silica on $Si_{0.2}$-Co_3O_4 solely results from sintering of the noncrystallized

DOI: 10.1021/acscatal.5b02900
ACS Catal. 2016, 6, 4218−4228

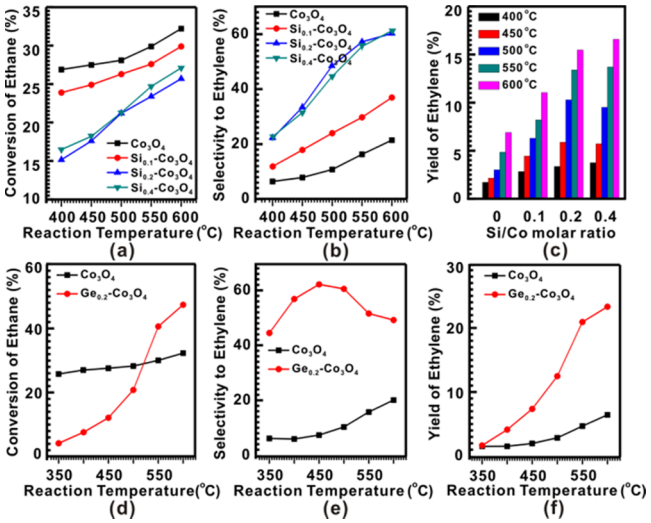

Figure 5. Catalytic activity, selectivity, and yield of (a–c) Si_x-Co_3O_4 (x = 0, 0.1, 0.2, 0.4) in the temperature range 400–600 °C and (d–f) $Ge_{0.2}$-Co_3O_4 catalyst in the temperature range 350–600 °C. The amount of each of the catalysts used here was 50 mg.

mesoporous silica at high temperature instead of any factors of catalysis, fresh $Si_{0.2}$-Co_3O_4 was directly annealed to 600 °C in O_2. As shown in Table 1, the surface area of the $Si_{0.2}$-Co_3O_4 after annealing at 600 °C in O_2 (112.1 m^2 g^{-1}) is similar to that of the $Si_{0.2}$-Co_3O_4 used in the ODH reaction at 600 °C (103.8 m^2 g^{-1}). This similarity suggests that the collapse of the mesoporous shell is only a thermal effect.

3.3. Catalytic Performances of Si_x-Co_3O_4. Figure 5a,b shows the catalytic activity and selectivity for ODH of ethane on pure Co_3O_4 and Si_x-Co_3O_4 (x = 0.1, 0.2, 0.4 in molar ratio). As displayed in Figure 5a,b, both the conversion of ethane and selectivity for production of ethylene strongly depend on the reaction temperature. The increase of catalytic conversion of ethane on each of the four catalysts suggests that the high reaction temperature enhances the overall reaction rate. At any temperature in the range of 400–600 °C, the conversion of ethane on pure Co_3O_4 is typically 5% higher than that of $Si_{0.1}$-Co_3O_4 even though the surface area of the used pure Co_3O_4 is lower than that of the used $Si_{0.1}$-Co_3O_4 by 43 m^2 g^{-1} (Figure 5a). It suggest a higher activity in conversion of ethane to products compared to $Si_{0.1}$-Co_3O_4. The obvious difference in catalytic selectivity in Figure 5b shows that the surface of $Si_{0.1}$-Co_3O_4 is obviously different from that of pure Co_3O_4.

The used $Si_{0.1}$-Co_3O_4 and used $Si_{0.2}$-Co_3O_4 have very similar surface areas (Table 1). However, they give different conversions of ethane (Figure 5a). In comparison to $Si_{0.1}$-Co_3O_4, the conversion of ethane on $Si_{0.2}$-Co_3O_4 is 5–10% lower in the temperature range of 400–600 °C, which can be rationalized by the "occupancy" effect of the collapsed silica shell. These collapsed silica shell terminated surface sites of Co_3O_4 decreased the catalytic activity of $Si_{0.2}$-Co_3O_4. However, there is no such occupancy effect for $Si_{0.1}$-Co_3O_4 since the $Si_{0.1}$-Co_3O_4 sample does not have an obvious shell.

Figure 5b presents the catalytic selectivity for production of ethylene through ODH of ethane on these four catalysts in the temperature range of 400–600 °C. All four catalysts including pure and doped Co_3O_4 catalysts exhibit the same temperature evolution of catalytic performance in terms of the increase in catalytic selectivity along with an increase in catalysis temperature. This is likely related to the hypothesis that ODH occurs through a hetero-homogeneous mechanism. Ethane molecules are activated on the surface of a catalyst, forming C_2H_5 species; the C_2H_5 species can react with very active species (O^-, O_2^- ,or O^{2-}) of the surface lattice of a catalyst to form OC_2H_5 intermediates. The O–C bond of the formed OC_2H_5 intermediates could be cleaved into C_2H_4 on the surface of the catalyst and then C_2H_4 would desorb as an ideal product. This is a mechanism of pure heterogeneous catalysis.[48] In addition, OC_2H_5 intermediates on the surface could be further oxidized by active oxygen species of the surface to form CO or CO_2; the pathways for the formation of CO or CO_2 are a pure heterogeneous mechanism as well.

The C_2H_5O intermediates formed on the surface could desorb to the gas phase and then dissociate into C_2H_4 through molecular collision in the gas phase at high temperature, called a radical-based pathway. Along with an increase of the catalysis temperature, the residence time of C_2H_5 species on the catalyst surface significantly decrease and thus a larger fraction of C_2H_5 or OC_2H_5 species desorb to the gas phase above the catalyst. From this point of view, the contribution of the pathway of collision and dissociation of radicals in the gas phase to form ethylene to the achieved selectivity of ethylene is greater at a higher temperature. Thus, the addition of a radical-based pathway in the gas phase to the heterogeneous catalysis (perfomed at the catalyst and gas interface) could rationalize the observed phenomena that selectivity for production of ethylene depends on the corresponding conversion of ethane since the conversion is higher at a higher temperature.

As shown in Figure 5b, the all doped Co_3O_4 catalysts exhibit a catalytic selectivity higher than that of pure Co_3O_4 by 20–40% in the temperature range of 400–600 °C. At any temperature in the temperature range of 400–600 °C, the catalytic selectivities of Co_3O_4, $Si_{0.1}$-Co_3O_4, and $Si_{0.2}$-Co_3O_4 increase along with the order of Co_3O_4, $Si_{0.1}$-Co_3O_4, and $Si_{0.2}$-Co_3O_4. The selectivity of $Si_{0.2}$-Co_3O_4 is higher than that of $Si_{0.1}$-Co_3O_4 by 12–30%. The selectvity of $Si_{0.1}$-Co_3O_4 is higher than that of pure Co_3O_4 by about 12%. Thus, doping of silicon atoms on Co_3O_4 can definitely increase the catalytic selectivity. Specifically, the selectivity of the $Si_{0.2}$-Co_3O_4 is twice as high as that of the pure Co_3O_4 at the same reaction temperature in the range of 400–600 °C by twice (6.3% of pure Co_3O_4 vs 20.0% of $Si_{0.2}$-Co_3O_4 at 400 °C; 20.4% of pure Co_3O_4 vs 61.3% of $Si_{0.2}$-Co_3O_4 at 600 °C) (Figure 5b). In addition, as shown in Figure 5c, the yields of ethylene on Si_x-Co_3O_4 are definitely higher than those on pure Co_3O_4 at all of the reaction temepratures. This significant increase in catalytic selectivity suggests a distinctly different surface of Si_x-Co_3O_4 in comparison to pure Co_3O_4.

As discussed above, the catalytic selectivity for production of ethylene very likely depends on the catalytic conversion of ethane due to the potential contribution of radical reactions in the gas phase. To confirm that the modified surface of Co_3O_4 by deposited silicon atoms does increase the catalytic selectivity for production of ethylene, we compared the selectivity of different catalysts at the same level of conversion at the same reaction temperature. As shown in Figure 6a,b, catalytic measurements of 65 mg of $Si_{0.2}$-Co_3O_4 and 50 mg of pure Co_3O_4 were performed in the temperature range of 400–600 °C in parallel. The conversions of ethane on the two catalysts at a temperature in the range of 500–600 °C are very similar. However, the selectivities of $Si_{0.2}$-Co_3O_4 and pure Co_3O_4 at a temperature in this temperature range are distinctly different (Figure 6b). For instance, the catalytic selectivity of $Si_{0.2}$-Co_3O_4 at 500 °C is higher than that of pure Co_3O_4 at this temperature by 26.0%

DOI: 10.1021/acscatal.5b02900
ACS Catal. 2016, 6, 4218–4228

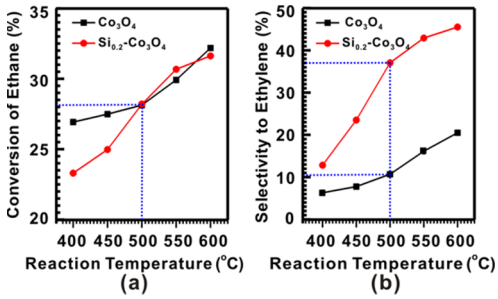

Figure 6. Comparison of catalytic selectivity for production of ethylene of Co_3O_4 and $Si_{0.2}$-Co_3O_4 under a similar conversion of ethane at a same temperature. (a) Conversion of ethane and (b) Selectivity to ethylene of Co_3O_4 and $Si_{0.2}$-Co_3O_4 at the temperature range (400 °C-600 °C) (0.065 g of $Si_{0.2}$-Co_3O_4 vs 0.050 g of Co_3O_4 were used for the catalysis). All these catalytic measurements were performed under the same condition as that described in Experimental Sections of the main text.

(10.0% vs 36.0%), though they have almost the same conversion of ethane (28.1%). These comparisons clearly show that the significant increase of catalytic selectivity of $Si_{0.2}$-Co_3O_4 does result from the intrinsic difference in surface structure between pure Co_3O_4 and Si-doped Co_3O_4. Moreover, to further understand the catalytic pathway, the contact time of $Si_{0.2}$-Co_3O_4 catalyst was changed. As shown in Figure 7, the

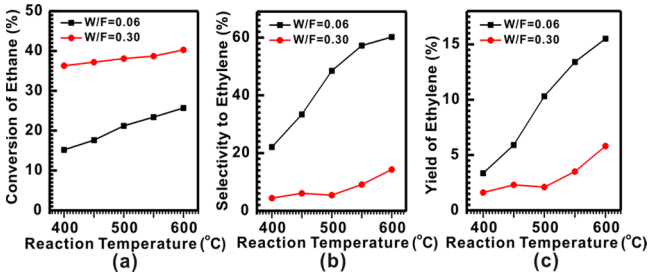

Figure 7. Catalytic activity (a), selectivity (b), and yield (c) of $Si_{0.2}$-Co_3O_4 at different contact time (at W/F = 0.06 g s mL^{-1}, the catalyst weight is 0.050 g diluted with 0.50 g of quartz sand, the flow rate of C_2H_6 (10%) is 25 mL min^{-1}, and the flow rate of O_2 (10%) is 25 mL min^{-1}; at W/F = 0.30 g s mL^{-1}, the catalyst weight is 0.050 g diluted with 0.50 g of quartz sand, the flow rate of C_2H_6 (10%) is 5.0 mL min^{-1}, and the flow rate of O_2 (10%) is 5.0 mL min^{-1}).

conversion of ethane is improved along with the increased W/F from 0.06 to 0.30 g s mL^{-1} (the contact time becomes longer), while the selectivity to ethylene decreased a great deal. In addition, the yield of ethylene decreased with an increase in the contact time. This clearly suggests that the reaction pathway is inclined to be consecutive.

3.4. Correlation between Catalytic Selectivity for Production of Ethylene and Activity of Surface Lattice Oxygen Atoms/Oxygen Vacancies. The difference in catalytic selectivity for the production of ethylene from ethane between pure Co_3O_4 and Si_x-Co_3O_4 clearly suggests that the surface of Si_x-Co_3O_4 is different from that of pure Co_3O_4. To further understand the difference in surfaces of pure Co_3O_4 and Si_x-Co_3O_4, H_2-TPR measurements were performed on them in parallel to investigate the difference in reduction properties. As shown in Figure 8a, a pure Co_3O_4 spectrum (the bottom one) shows two main reduction peaks around 250 °C (the sharp peak is marked with black dashed line) and 500 °C (the broader peak is marked with a light green dashed line), which are attributed to

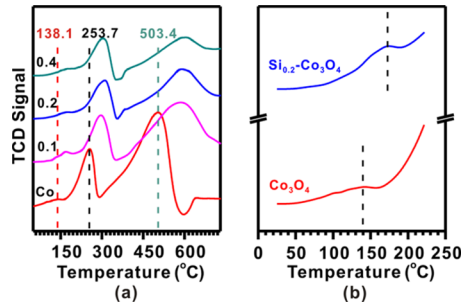

Figure 8. (a) H_2-TPR spectra of Si_x-Co_3O_4 (x = 0, 0.1, 0.2, 0.4) and (b) enlargement of the spectra of $Si_{0.2}$-Co_3O_4 and pure Co_3O_4 in the temperature range of 20−225 °C.

the reduction of Co_3O_4 to CoO and of CoO to Co, respectively.[49−51] In comparison to pure Co_3O_4, the reduction behaviors of $Si_{0.1}$-Co_3O_4, $Si_{0.2}$-Co_3O_4, and $Si_{0.4}$-Co_3O_4 are quite different. The doping of silicon atoms on the surface of Co_3O_4 results in a shift of the two reduction temperatures to higher values, suggesting that the reduction of Co_3O_4 of Si_x-Co_3O_4 to CoO and of CoO to Co is suppressed by the doping of silicon atoms. In addition to the two major reduction peaks, a small peak at about 140−200 °C was observed on Si_x-Co_3O_4 (see blue line in Figure 8b), which could be assigned to the reduction of surface lattice oxygen.[52] It can be seen from Figure 8b that the reduction temperature of the surface lattice oxygen on pure Co_3O_4 is 138 °C which is lower than that of Si_x-Co_3O_4 (170 °C), suggesting that doping of silicon atoms on the Co_3O_4 surface has suppressed the removal of surface lattice oxygen of Si_x-Co_3O_4.

In order to confirm whether the doped silicon atoms can affect the activity of surface lattice oxygen atoms/oxygen vacancies of Co_3O_4, the oxygen isotope-exchange experiments were performed on isotoped labeled catalysts $Co_3{}^{16}O_{4-x}{}^{18}O^8{}_x$ and $Si_{0.2}$-$Co_3{}^{16}O_{4-x}{}^{18}O_x$. The advantage of the present temperature programmed isotope exchange to investigate the isotope exchange is that we can get the isotopic exchange signal clearly and separately. This is because the isotope exchange is a relative slow process which requires a longer time to achieve the equilibrium. If we use the conventional temperature program of the linear heating, the isotopic exchange signal are likely concealed by the linear heating (20 °C min^{-1}) and overlap each other. Comparing to conventional temperature program of linear heating, the present temperature program enables enough time for isotope exchange and thus achieves a good recognition of the isotope exchange.

Before isotope-exchange experiments, the isotope-labeled catalysts $Co_3{}^{16}O_{4-x}{}^{18}O_x$ and $Si_{0.2}$-$Co_3{}^{16}O_{4-x}{}^{18}O_x$ were prepared by annealing Co_3O_4 or $Si_{0.2}$-Co_3O_4 in $^{18}O_2$ for 30 min. Then, the prepared $Co_3{}^{16}O_{4-x}{}^{18}O_x$ or $Si_{0.2}$-$Co_3{}^{16}O_{4-x}{}^{18}O_x$ was located in a fixed-bed flow reactor. A 30 mL min^{-1} flow of ∼5% $^{16}O_2$ was passed through the isotope-labeled catalysts. The gas downstream of this reactor was sampled at a high-vacuum chamber through a quartz capillary between the fixed-bed flow reactor and the high-vacuum chamber. This high-vacuum chamber was equipped with a mass spectrometer. The catalyst in the reactor was annealed from 30 to 600 °C with a ramping rate of 20 °C min^{-1} while 5% $^{16}O_2$ was continuously flowing through the isotope-labeled catalyst. Once one of the gaseous products of isotope exchange, $^{16}O^{18}O$ (m/z 34), was observed at T_0 (Figure 9), the annealing of the catalyst continued to the highest intensity of the $^{16}O^{18}O$ signal in the mass spectrum at a temperature marked as T_m; then the catalyst was maintained at T_m until the

DOI: 10.1021/acscatal.5b02900
ACS Catal. 2016, 6, 4218−4228

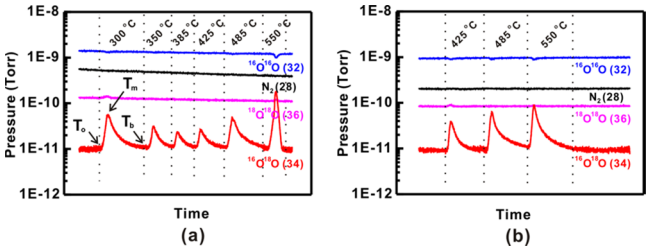

Figure 9. Mass spectra of $^{16}O^{18}O$ on $Co_3{}^{16}O_{4-x}{}^{18}O_x$ or $Si_{0.2}$-$Co_3{}^{16}O_{4-x}{}^{18}O_x$ in the temperature range of 30−600 °C recorded during the exchange of surface oxygen atoms of catalysts with flowing $^{16}O_2$: (a) $Co_3{}^{16}O_{4-x}{}^{18}O_x$; (b) $Si_{0.2}Co_3{}^{16}O_{4-x}{}^{18}O_x$.

$^{16}O^{18}O$ signal compeletely decayed to the baseline of $^{16}O^{18}O$. Then, the sample was continuously annealed with the normal ramping rate 20 °C min^{-1}. During this experiment, oxygen vacancies of surface of pure Co_3O_4 can readily dissociate molecular oxygen ($^{16}O^{16}O$) of the flowing gas $^{6}O^{16}O$ and thus the isotope exchange *between* ^{16}O atoms generated from dissociating the freshly introduced $^{16}O^{16}O$ *and* the original surface ^{18}O atoms can occur. Six and three peaks of $^{16}O^{18}O$ were observed in the mass spectra of pure Co_3O_4 (Figure 9a) and $Si_{0.2}$-Co_3O_4 (Figure 9b), respectively. For instance, six peaks (T_m) of $^{16}O^{18}O$ at 300, 350, 385, 425, 485, and 550 °C were observed from pure Co_3O_4 (Figure 9a). In comparison to the pure Co_3O_4, no peak of $^{16}O^{18}O$ at a temperature lower than 400 °C was observed on $Si_{0.2}$-Co_3O_4 under the exactly same experimental condition as pure Co_3O_4, although peaks at 425, 485, and 550 °C were observed clearly (Figure 9b). This difference suggests that the capability of Co_3O_4 in dissociating molecular oxygen is greatly weakened through doping silicon atoms on the surface lattice of Co_3O_4. This pinning effect of doped silicon atoms on surface lattice oxygen atoms makes $Si_{0.2}$-Co_3O_4 have a lower capability to release surface lattice oxygen atoms and to dissociate molecular oxygen on oxygen vacancies. This difference in the capability in releasing surface lattice oxygen atoms and dissociating molecular oxygen can rationalize the difference in catalytic activities for a complete oxidation of ethane to CO_2 and H_2O on pure Co_3O_4 and $Si_{0.2}$-Co_3O_4, as discussed in the following.

To further confirm the difference in activities of surface lattice oxygen atoms/oxygen vacancies between the pure Co_3O_4 and doped Co_3O_4, the complete oxidations of ethane on the two catalysts were performed. Figure 10 presents the conversion of ethane in the complete oxidation of ethane to CO_2 and H_2O on $Si_{0.2}$-Co_3O_4 and pure Co_3O_4 in a mixture of ethane and oxygen

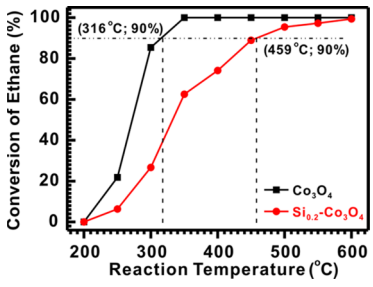

Figure 10. Catalytic performance of deep oxidation of ethane on $Si_{0.2}$-Co_3O_4 and pure Co_3O_4 (W/F = 0.06 g s mL^{-1}; the catalyst weight is 0.050 g diluted with 0.50 g quartz sand, the flow rate of C_2H_6 (10%) is 10 mL min^{-1}, and the flow rate of O_2 (10%) is 40 mL min^{-1}).

with a molecular ratio of 1:4. Even though the surface area of the used pure Co_3O_4 is smaller than that of the used $Si_{0.2}$-Co_3O_4 (Table 1), the conversion of ethane on pure Co_3O_4 is higher than that on $Si_{0.2}$-Co_3O_4. The temperature at which 90% of C_2H_6 was converted on $Si_{0.2}$-Co_3O_4 is 459 °C, which is definitely higher than that of 316 °C on pure Co_3O_4 (Figure 10). Thus, pure Co_3O_4 is definitely more active than $Si_{0.2}$-Co_3O_4 in the complete oxidation of ethane. This further suggests that the activity of surface lattice oxygen of $Si_{0.2}$-Co_3O_4 is lower at the same temperature. The suppression of activity in oxidation after doping of silicon (evidenced from the complete oxidation of ethane in Figure 10) is consistent with the increase of selectivity for the production of ethylene by pinning some surface oxygen species active for deep oxidation to CO or/and CO_2.

3.5. Application of this Method To Promote Catalytic Selectvity by Using Another Nonmetallic Element. To explore whether this method of increasing catalytic selectivity by doping atoms of a nonmetallic element can be applied to other cases, Ge was doped on the surface lattice of pure Co_3O_4. Figure 4e,f presents photoemission features of Co 2p and Ge 3d of Ge-doped Co_3O_4. Similar to the influence of doped Si on the photoemission features of Co 2p, the doped Ge atoms make Co 2p of $Ge_{0.2}$-Co_3O_4 upshift by 1.3 eV in comparison to Co 2p of pure Co_3O_4. Notably, Ge 3d of $Ge_{0.2}$-Co_3O_4 downshifts with respect to the Ge 3d of GeO_2.[53] The similarity of Ge 3d photemission peaks of of $Ge_{0.2}$-Co_3O_4 and GeO_2 supported on Ge suggests that the doped Ge atoms replace Co instead of O atoms of Co_3O_4. If oxygen atoms on the Co_3O_4 surface were replaced by Ge atoms, Ge atoms must have bonded to Co atoms, and Ge atoms should have definitely downshifted due to the low electronegativity of Co in comparison to that of O. Thus, the photoemission features of Co 2p and Ge 3d in Figures 4a and 4f suggest that Ge atoms replace Co and thus bond with oxygen atoms.

Catalytic performances of 50 mg of Ge-doped Co_3O_4 and 50 mg of pure Co_3O_4 were measured under the same conditions as for Si_x-Co_3O_4. A 50 mg of Ge-doped Co_3O_4 and 50 mg of pure Co_3O_4 exhibit similar conversions at a temperature between 500 and 550 °C in Figure 5d. However, at this temperature Ge-doped Co_3O_4 exhibits much higher catalytic selectivity by 35−52% than pure Co_3O_4 in Figure 5e. As shown in Figure 5f, the yield of the ethylene on Ge-doped Co_3O_4 is also higher than that on pure Co_3O_4. Notably, the distinctly different catalytic selectivities between 500 and 550 °C while their conversions are very similar (Figure 5d) clearly show that the promotion effect in catalytic selectivity results from the doping of Ge.

3.6. Understanding the Promotion Effect in Selectivity of ODH through Computational Studies. Computational studies were performed to interpret how the doping of silicon atoms suppresses the complete oxidation of ethane and thus enhances the selectivity for production of ethylene through ODH. Imaging the used catalyst nanoparticles of $Si_{0.2}$-Co_3O_4 with aberration-corrected STEM shows that the preferentially exposed facet is (111) (Figure 2l). Thus, the (111) surface was chosen as the surface of pure Co_3O_4 and doped Co_3O_4 for the following computational studies. Figures 11a and 11b give the structural models of Si-doped Co_3O_4 and pure Co_3O_4, respectively. Figure 11c shows the (111) surface of doped Co_3O_4. On the surface of the structural model of Si_x-Co_3O_4, Si atoms replace cobalt atoms. As an OH group can strongly bond on the Si atom of silica at temperatures as high as 700−800 °C,[54−56] it was used to terminate the doped silicon atom (Figure 11b). Three oxygen atoms near Si atoms denoted O^1, O^2, and O^3

DOI: 10.1021/acscatal.5b02900
ACS Catal. 2016, 6, 4218−4228

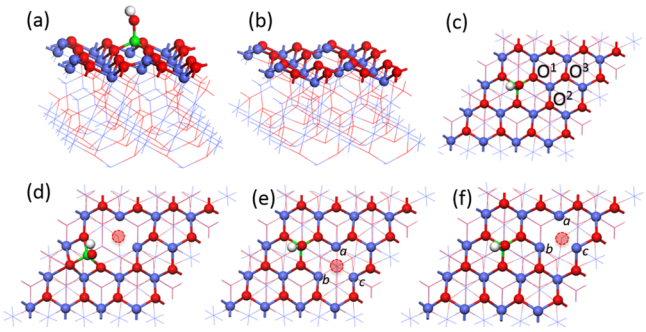

Figure 11. Optimized structural models of pure Co_3O_4 and $Si_{0.2}$-Co_3O_4 for calculations. (a) Structural model of $Si_{0.2}$-Co_3O_4. (b) Structural model of pure Co_3O_4. (c) Surface structure of (111) of $Si_{0.2}$-Co_3O_4. (d–f) Three types of oxygen vacancies on (111) of $Si_{0.2}$-Co_3O_4 were formed by removing O^1, O^2, or O^3 of (c). In this figure, blue, red, green, and white represent Co, O, Si, and H atoms, respectively. The pink spots in (d–f) represent oxygen vacancies.

are chosen as surface lattice oxygen atoms of Si_x-Co_3O_4 (Figure 11c). By removing any of them, three types of oxygen vacancies can be created (Figure 11d–f). The oxygen vacancy in Figure 11d was created by taking away O^1 directly bonding to the Si atom. However, upon a structural optimization the silicon atom of the surface structure significantly offsets from its original position. In our opinion, such an oxygen vacancy with significantly offset neighboring cobalt atoms (Figure 11d) cannot represent the surface Si_x-Co_3O_4 and thus was not considered in our simulation. As shown in Figure 11e,f, the bonding configurations of Co^a, Co^b, and Co^c near to the oxygen vacancy do not change significantly after removal of O^2 or O^3. Thus, surface structures in Figure 11e,f were used as active surfaces in the following theoretical simulation.

Our isotope experiments discussed above indicated the difference in activity of surface lattice oxygen atoms/oxygen vacancies between the pure Co_3O_4 and doped Co_3O_4. To understand this key difference, we compared pure Co_3O_4 and doped Co_3O_4 in terms of mobility of the surface vacancies and their activities in dissociating O_2. We first examine O_2 dissociation on oxygen vacancies. As shown in Figure 12a, the barrier for the dissociation of O_2 on pure Co_3O_4 is about 0.52 eV (the initial structure, the transition state, and the final structure are shown in Figure 12b–d, respectively). However, the barrier is about 0.85 eV on Si-Co_3O_4 (Figure 12e). The initial structure, the transition state, and the final structure are shown in Figure 12f–h, respectively. The higher barrier on Si-doped Co_3O_4 suggests the obvious decrease of the activity of surface oxygen vacancies in dissociating molecular O_2 in comparison to the case for pure Co_3O_4. This is consistent with the experimental observation that no isotope exchange could occur on $Si_{0.2}$-Co_3O_4 at temperatures below 425 °C (Figure 9b) although exchange did occur on pure Co_3O_4 at 300, 350, and 385 °C (Figure 9a).

Hopping of surface oxygen vacancies is considered as another scale to evaluate the activity of surface oxygen vacancies. If an energy barrier requested for hopping one vacancy to another location of a surface is low, this surface typically has a high activity in generation of surface oxygen vacancies. The energy barriers for an oxygen vacancy hopping on Co_3O_4(111) and Si-doped Co_3O_4 (111) were calculated. As shown in Figure 13, the energy barrier is about 2.70 eV of Si-doped Co_3O_4 (111) (Figure 13a; the initial structure, the transition state, and the final structure are shown in Figure 13b–d, respectively), much higher than 1.30 eV for the pure Co_3O_4 (111) surface (Figure 13e; the initial

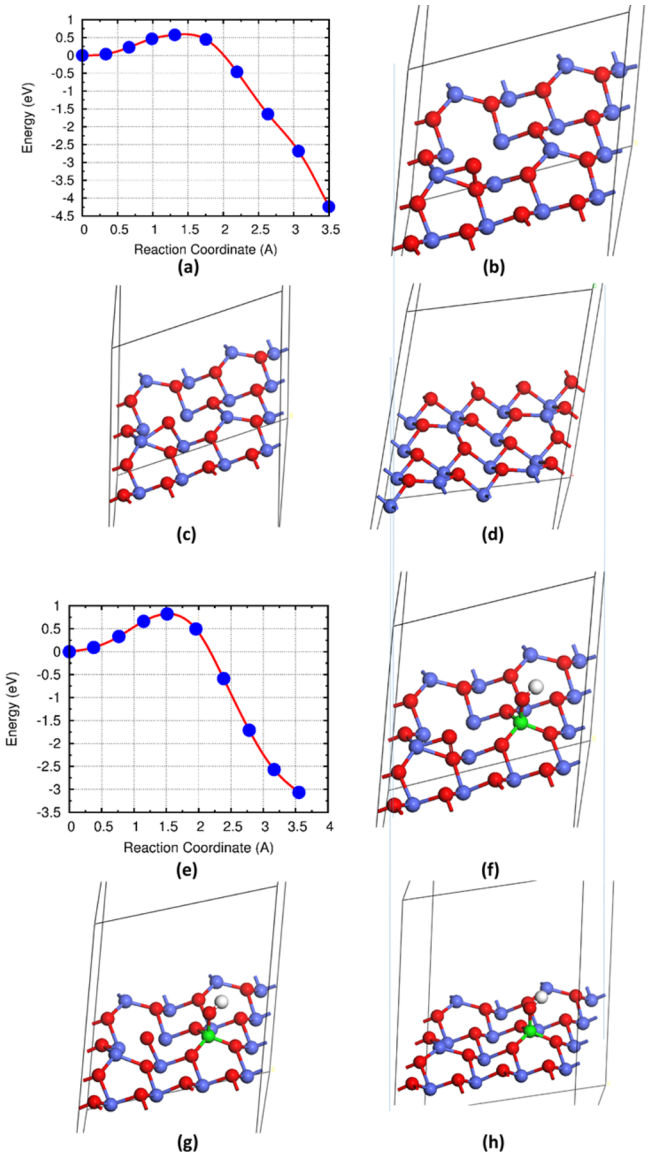

Figure 12. Energy profile for dissociation of molecular O_2 on surface oxygen vacancies on pure Co_3O_4 and Si-doped Co_3O_4. (a) Evolution of energy in dissociation of molecular oxygen on pure Co_3O_4 along reaction coordination. (b–d) Initial structure, transition state, and final structure of pure Co_3O_4 for dissociation of O_2, respectively. (e) Evolution of energy in the dissociation of molecular oxygen on Si-doped Co_3O_4 along reaction coordination. (f–h) Initial structure, transition state, and final structure of Si-doped Co_3O_4 for dissociation of O_2, respectively.

structure, the transition state, and the final structure are shown in Figure 13f–h, respectively). This further suggests the suppression of the mobility of surface oxygen vacancies by silicon.

Our computed energy profiles for O_2 dissociation on surface oxygen vacancies and the mobility of surface oxygen vacancies confirmed our experimental observation that doping Si atoms on the surface lattice of Co_3O_4 suppresses the activity of surface lattice oxygen. Here we note that this computational finding results from the calculations of the (111) surface of Co_3O_4, suggested from our STEM images. The activity of Co_3O_4 may depend on the crystallographic surfaces: in other words, the packing of Co and O ions on the surface of Co_3O_4. For instance, it has been shown in a previous DFT work that on the more

DOI: 10.1021/acscatal.5b02900
ACS Catal. 2016, 6, 4218–4228

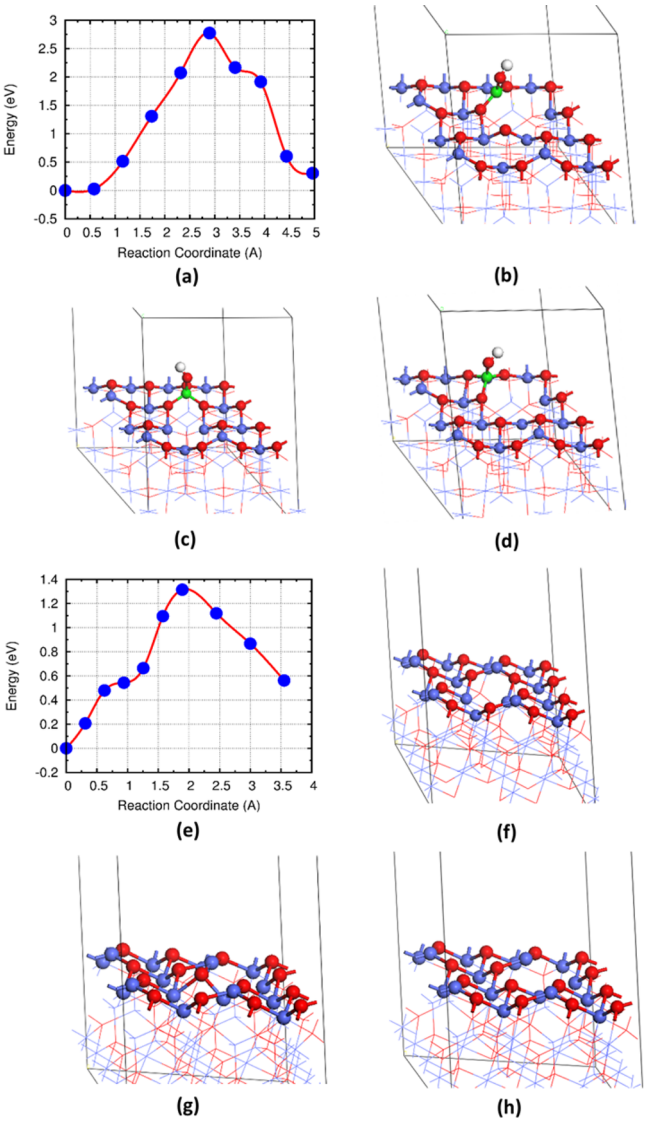

Figure 13. Energy profile for a surface oxygen vacancy (dashed circle) to hop to a neighboring oxygen site on Si-doped Co_3O_4 and pure Co_3O_4. (a) Evolution of energy in hopping a surface oxygen vacancy on Si-doped Co_3O_4 along reaction coordination. (b–d) Initial structure, transition state, and final structure of Si-doped Co_3O_4 in this hopping process. (e) Evolution of energy in hopping a surface oxygen vacancy on pure Co_3O_4 along reaction coordination. (f–h) Initial structure, transition state, and final structure of pure Co_3O_4 in this hopping process.

closely packed Co_3O_4(110)-B surface the barrier for vacancy hopping could be as low as 0.26 eV and O_2 dissociation could also be facile.[57]

3.7. Durability of Catalytic Performance and Reusability of Si-doped Co_3O_4. The durability of catalytic activity and selectivity of ODH on $Si_{0.2}$-Co_3O_4 was examined by maintaining the catalyst at 600 °C for 100 h under the catalytic reaction conditions while its catalytic activity and selectivity were continuously monitored with online measurements by gas chromatography. As shown in Figure 14a, the catalytic selectivity and conversion of $Si_{0.2}$-Co_3O_4 were maintained at ~63% and ~26%, respectively, over the entire time span of the durability test. In addition, the reusability of $Si_{0.2}$-Co_3O_4 was tested. There are only subtle changes during repetition of four continuous

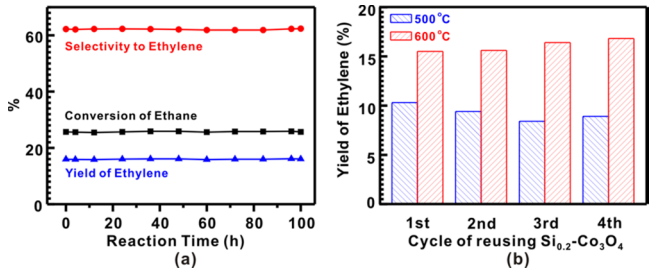

Figure 14. Catalytic performance of $Si_{0.2}$-Co_3O_4 in tests of durability and reusability. (a) Conversion, selectivity, and yield at 600 °C as a function of time over the first 100 h. (b) Plot of yields of ethylene in the first four cycles of test of reusability at 500 and 600 °C (experimental conditions: W/F = 0.06 g s mL^{-1}; catalyst weight 0.050 g diluted with 0.50 g of quartz sand; flow rate of C_2H_6 (10%) 25 mL min^{-1}; flow rate of O_2 (10%) 25 mL min^{-1}).

cycles, as shown in Figure 14b. This suggests that the $Si_{0.2}$-Co_3O_4 catalyst has a quite high stability in the ODH of ethane.

4. CONCLUSION

Our studies demonstrated that tuning of the activity of surface lattice oxygen/oxygen vacancies through depositing atoms of nonmetallic elements on the surface lattice of metal oxide is a new approach for promoting catalytic selectivity by suppression of side-reaction channels of deep oxidations such as a complete oxidation of the reactant. Catalytic performances and surfaces of catalysts of silicon-doped Co_3O_4, Si_x-Co_3O_4 (x = 0.1, 0.2, 0.4), were studied toward a fundamental understanding of the *correlation* of the catalytic selectivity of ODH for production of ethylene *with* the capability of providing active atomic oxygen on the surface of Co_3O_4. Si_x-Co_3O_4 exhibits a high selectivity for production of ethylene, which is twice as high as that of pure Co_3O_4 under the same catalytic conditions. This significant promotion of catalytic selectivity for production of ethylene in ODH results from the increases in activation barriers of dissociating molecular O_2 on surface oxygen vacancies and pinning certain type of very active surface oxygen species through doping of silicon atoms on the surface lattice of Co_3O_4. In addition, this new method of significantly promoting catalytic selectivity was supported by the observation of much higher selectivity of Ge-doped Co_3O_4 in comparison to pure Co_3O_4.

AUTHOR INFORMATION

Corresponding Authors

*E-mail for J.F.: jfan@zju.edu.cn.
*E-mail for F.T.: franklin.feng.tao@ku.edu.

Author Contributions

⊥Those authors made equal contributions.

Notes

The authors declare no competing financial interest.

ACKNOWLEDGMENTS

Both experimental and theoretical studies were solely supported by the Chemical Sciences, Geosciences and Biosciences Division, Office of Basic Energy Sciences, Office of Science, U.S. Department of Energy, under Grant No. DE-SC0014561. The authors appreciate Yuheng Zhou for aid in XPS and XRD experiments of Co_3O_4 and Si_x-Co_3O_4 samples. J.L. appreciates a scholarship from the China Scholarship Council. This research used resources of the National Energy Research Scientific Computing Center, a DOE Office of Science User Facility

DOI: 10.1021/acscatal.5b02900
ACS Catal. 2016, 6, 4218–4228

supported by the Office of Science of the U.S. Department of Energy under Contract No. DE-AC02-05CH11231.

REFERENCES

(1) Matsubu, J. C.; Yang, V. N.; Christopher, P. *J. Am. Chem. Soc.* **2015**, *137*, 3076−3084.
(2) Wang, H.; Wang, Y.; Zhu, Z.; Sapi, A.; An, K.; Kennedy, G.; Michalak, W. D.; Somorjai, G. A. *Nano Lett.* **2013**, *13*, 2976−2979.
(3) Liu, S.-S.; Sun, K.-Q.; Xu, B.-Q. *ACS Catal.* **2014**, *4*, 2226−2230.
(4) Liu, R.; Huang, H.; Li, H.; Liu, Y.; Zhong, J.; Li, Y.; Zhang, S.; Kang, Z. *ACS Catal.* **2014**, *4*, 328−336.
(5) Tao, F. F.; Shan, J.-j.; Nguyen, L.; Wang, Z.; Zhang, S.; Zhang, L.; Wu, Z.; Huang, W.; Zeng, S.; Hu, P. *Nat. Commun.* **2015**, *6*, 7798.
(6) Artiglia, L.; Agnoli, S.; Savio, L.; Pal, J.; Celasco, E.; Rocca, M.; Bondino, F.; Magnano, E.; Castellarin-Cudia, C.; Netzer, F. P.; Granozzi, G. *ACS Catal.* **2014**, *4*, 3715−3723.
(7) Kondratenko, V. A.; Berger-Karin, C.; Kondratenko, E. V. *ACS Catal.* **2014**, *4*, 3136−3144.
(8) Jin, X.; Dang, L.; Lohrman, J.; Subramaniam, B.; Ren, S.; Chaudhari, R. V. *ACS Nano* **2013**, *7*, 1309−1316.
(9) Ksar, F.; Ramos, L.; Keita, B.; Nadjo, L.; Beaunier, P.; Remita, H. *Chem. Mater.* **2009**, *21*, 3677−3683.
(10) Tang, Y.; Xu, S.; Dai, Y.; Yan, X.; Li, R.; Xiao, L.; Fan, J. *Chem. Commun.* **2014**, *50*, 213−215.
(11) Tritsaris, G. A.; Rossmeisl, J. *J. Phys. Chem. C* **2012**, *116*, 11980−11986.
(12) Sattler, J. J. H. B.; Ruiz-Martinez, J.; Santillan-Jimenez, E.; Weckhuysen, B. M. *Chem. Rev.* **2014**, *114*, 10613−10653.
(13) Schweitzer, N. M.; Hu, B.; Das, U.; Kim, H.; Greeley, J.; Curtiss, L. A.; Stair, P. C.; Miller, J. T.; Hock, A. S. *ACS Catal.* **2014**, *4*, 1091−1098.
(14) Otsuka, K.; Jinno, K.; Morikawa, A. *J. Catal.* **1986**, *100*, 353−359.
(15) Cundall, R. B.; Fussey, D. E.; Harrison, A. J.; Lampard, D. *J. Chem. Soc., Faraday Trans. 1* **1979**, *75*, 1390−1394.
(16) Chen, Q.; Schweitzer, E. J. A.; Van Den Oosterkamp, P. F.; Berger, R. J.; De Smet, C. R. H.; Marin, G. B. *Ind. Eng. Chem. Res.* **1997**, *36*, 3248−3251.
(17) Xu, C.; Al Shoaibi, A. S.; Wang, C.; Carstensen, H.-H.; Dean, A. M. *J. Phys. Chem. A* **2011**, *115*, 10470−10490.
(18) Ducarme, V.; Martin, G. A. *Catal. Lett.* **1994**, *23*, 97−101.
(19) Cavani, F.; Trifirò, F. *Catal. Today* **1995**, *24*, 307−313.
(20) Glasier, G. F.; Pacey, P. D. *Carbon* **2001**, *39*, 15−23.
(21) Savova, B.; Loridant, S.; Filkova, D.; Millet, J. M. M. *Appl. Catal., A* **2010**, *390*, 148−157.
(22) Lee, W. J.; Li, C.-Z. *Appl. Catal., A* **2007**, *316*, 90−99.
(23) Shah, N.; Wang, Y.; Panjala, D.; Huffman, G. P. *Energy Fuels* **2004**, *18*, 727−735.
(24) Heracleous, E.; Lemonidou, A. A. *J. Catal.* **2006**, *237*, 162−174.
(25) Zhu, H.; Ould-Chikh, S.; Anjum, D. H.; Sun, M.; Biausque, G.; Basset, J.-M.; Caps, V. *J. Catal.* **2012**, *285*, 292−303.
(26) Solsona, B.; Concepción, P.; Demicol, B.; Hernández, S.; Delgado, J. J.; Calvino, J. J.; López Nieto, J. M. *J. Catal.* **2012**, *295*, 104−114.
(27) Zhu, H.; Rosenfeld, D. C.; Anjum, D. H.; Sangaru, S. S.; Saih, Y.; Ould-Chikh, S.; Basset, J.-M. *J. Catal.* **2015**, *329*, 291−306.
(28) Skoufa, Z.; Heracleous, E.; Lemonidou, A. A. *J. Catal.* **2015**, *322*, 118−129.
(29) Zhu, H.; Rosenfeld, D. C.; Anjum, D. H.; Caps, V.; Basset, J.-M. *ChemSusChem* **2015**, *8*, 1254−1263.
(30) Botella, P.; Dejoz, A.; López Nieto, J. M.; Concepción, P.; Vázquez, M. I. *Appl. Catal., A* **2006**, *298*, 16−23.
(31) Valente, J. S.; Armendáriz-Herrera, H.; Quintana-Solórzano, R.; del Ángel, P.; Nava, N.; Massó, A.; López Nieto, J. M. *ACS Catal.* **2014**, *4*, 1292−1301.
(32) Ruth, K.; Burch, R.; Kieffer, R. *J. Catal.* **1998**, *175*, 27−39.
(33) Zhu, H.; Laveille, P.; Rosenfeld, D. C.; Hedhili, M. N.; Basset, J.-M. *Catal. Sci. Technol.* **2015**, *5*, 4164−4173.
(34) Skoufa, Z.; Xantri, G.; Heracleous, E.; Lemonidou, A. A. *Appl. Catal., A* **2014**, *471*, 107−117.
(35) Zhou, Q.; Zhou, D.; Wu, Y.; Wu, T. *J. Rare Earths* **2013**, *31*, 669−673.
(36) Zhu, H.; Dong, H.; Laveille, P.; Saih, Y.; Caps, V.; Basset, J.-M. *Catal. Today* **2014**, *228*, 58−64.
(37) Xie, X.; Shang, P.; Liu, Z.; Lv, Y.; Li, Y.; Shen, W. *J. Phys. Chem. C* **2010**, *114*, 2116−2123.
(38) Xie, X.; Li, Y.; Liu, Z.-Q.; Haruta, M.; Shen, W. *Nature* **2009**, *458*, 746−749.
(39) Kresse, G.; Furthmuller, J. *Phys. Rev. B: Condens. Matter Mater. Phys.* **1996**, *54*, 11169−11186.
(40) Dudarev, S. L.; Botton, G. A.; Savrasov, S. Y.; Humphreys, C. J.; Sutton, A. P. *Phys. Rev. B: Condens. Matter Mater. Phys.* **1998**, *57*, 1505−1509.
(41) Perdew, J. P.; Burke, K.; Ernzerhof, M. *Phys. Rev. Lett.* **1996**, *77*, 3865−3868.
(42) Blochl, P. E. *Phys. Rev. B: Condens. Matter Mater. Phys.* **1994**, *50*, 17953−17979.
(43) Nagarajan, V. S.; Rao, K. J. *J. Mater. Sci.* **1989**, *24*, 2140−2146.
(44) Chuang, T.; Brundle, C.; Rice, D. *Surf. Sci.* **1976**, *59*, 413−429.
(45) Zhang, S.; Shan, J.; Zhu, Y.; Nguyen, L.; Huang, W.; Yoshida, H.; Takeda, S.; Tao, F. *Nano Lett.* **2013**, *13*, 3310−3314.
(46) Joo, S. H.; Park, J. Y.; Tsung, C.-K.; Yamada, Y.; Yang, P.; Somorjai, G. A. *Nat. Mater.* **2009**, *8*, 126−131.
(47) Wen, C.; Zhu, Y.; Ye, Y.; Zhang, S.; Cheng, F.; Liu, Y.; Wang, P.; Tao, F. *ACS Nano* **2012**, *6*, 9305−9313.
(48) Chen, T.; Li, W.-Z.; Zhang, J.-F.; Wu, Y.; Cao, X.-D.; Wan, H.-L. *Acta Chim. Sinica* **2004**, *62*, 1760−1764.
(49) Deng, J.; Zhang, L.; Dai, H.; Xia, Y.; Jiang, H.; Zhang, H.; He, H. *J. Phys. Chem. C* **2010**, *114*, 2694−2700.
(50) Wang, C.-B.; Tang, C.-W.; Gau, S.-J.; Chien, S.-H. *Catal. Lett.* **2005**, *101*, 59−63.
(51) Wang, H.; Ye, J. L.; Liu, Y.; Li, Y. D.; Qin, Y. N. *Catal. Today* **2007**, *129*, 305−312.
(52) Song, W.; Poyraz, A. S.; Meng, Y.; Ren, Z.; Chen, S.-Y.; Suib, S. L. *Chem. Mater.* **2014**, *26*, 4629−4639.
(53) John, F. M.; Stickle, W. F.; Sobol, P. E.; Bomben, K. D. *Handbook of X-ray Photoelectron Spectroscopy*; Perklin-Elmer Corportation: Minneapolis, MN, 1992; p 88.
(54) Falcaro, P.; Grosso, D.; Amenitsch, H.; Innocenzi, P. *J. Phys. Chem. B* **2004**, *108*, 10942−10948.
(55) Miyazaki, S.; Hamamoto, Y.; Yoshida, E.; Ikeda, M.; Hirose, M. *Thin Solid Films* **2000**, *369*, 55−59.
(56) Sneh, O.; George, S. M. *J. Phys. Chem.* **1995**, *99*, 4639−4647.
(57) Zhan, C.; Zhang, Y.; Cummings, P. T.; Jiang, D.-e. *Phys. Chem. Chem. Phys.* **2016**, *18*, 4668−4674.

DOI: 10.1021/acscatal.5b02900
ACS Catal. 2016, 6, 4218−4228